

Heterostructure of a 2.5 THz range quantum-cascade detector

© A.V. Babichev¹, E.S. Kolodeznyi¹, A.G. Gladyshev¹, D.V. Denisov², A. Jollivet³, P. Quach³,
L.Ya. Karachinsky^{1,4,5}, V.N. Nevedomsky⁴, I.I. Novikov^{1,5}, M. Tchernycheva³, F.H. Julien³, A.Yu. Egorov⁵

¹ ITMO University,

197101 St. Petersburg, Russia

² St. Petersburg Electrotechnical University „LETI“,

197022 St. Petersburg, Russia

³ Centre de Nanosciences et de Nanotechnologies (C2N), UMR 9001 CNRS, Université Paris-Saclay,

91120 Palaiseau, France

⁴ Ioffe Institute,

194021 St. Petersburg, Russia

⁵ Connector Optics LLC,

194292 St. Petersburg, Russia

E-mail: a.babichev@mail.ioffe.ru

Received October 15, 2021

Revised October 29, 2021

Accepted October 29, 2021

The design of the heterostructure of a 2.5 THz range quantum-cascade detector is proposed and heterostructure is grown by molecular-beam epitaxy technique. To optimize the thicknesses of the layers of the heterostructure cascades, a numerical method for iterative solution of the Schrödinger–Poisson equation in the $k \cdot p$ formalism was used. The grown heterostructure of the quantum-cascade detector showed a high structural perfection, confirmed by the small values of the average FWHM of the high-order satellite peaks on the X-ray diffraction rocking curves, which were $(8.3 \pm 0.5)^\circ$. Analysis of dark-field images obtained by transmission electron microscopy showed that the total thickness of the layers in the cascade is (137.3 ± 6.9) nm, which corresponds to the calculated thickness of the layers in the cascade of the heterostructure of the quantum-cascade detector.

Keywords: superlattices, quantum-cascade detector, epitaxy, gallium arsenide

DOI: 10.21883/SC.2022.03.53069.9750

1. Introduction

Terahertz (THz) spectroscopy may ensure a higher sensitivity as compared with the near IR spectrum spectroscopy due to vibration-rotation absorption lines in the terahertz spectrum of some molecules. THz spectroscopy applications include production process control [1], environmental analysis [2], and health assessment [3,4]. Due to large geometrical dimensions and high cost, commercial THz time-domain spectroscopy systems (THz TDS) [5] have not been widely used, moreover, their performance in a frequency band higher than 2 THz is very limited.

One of the prospective approaches to the development of space-saving THz spectroscopy systems includes the development of dual-comb spectroscopy (DCS) on the basis of quantum-cascade lasers (QCL) [1]. By now THz QCL with high optical output have been demonstrated. They are designed for operation at temperatures up to 250 K [6] and have wide intensification range to ensure considerable wavelength-tuning required for THz comb spectroscopy.

Though high-speed near-infrared [7] and medium-infrared [8] (IR) detectors are available, the lack of high-speed far-IR (THz) detectors with chip integration capability imposes considerable restrictions on the development of space-saving dual-comb spectroscopy systems.

Due to short carrier lives, semiconductor quantum-confined intersubband THz detectors are very promising

for implementation of high-speed detectors. IR quantum well infrared photodetectors (QWIP) show high detecting performance in THz frequency band compared with bolometer sensitivity [9]. However, there are physical restrictions imposed on THz QWIP at room temperature. Moreover, high-speed QWIPs (cutoff frequency 70 GHz) were demonstrated at $\sim 10 \mu\text{m}$ wavelengths [8]. At the same time, quick response of THz QWIP does not exceed 4.3 GHz [10,11]. The applications of THz QCL heterostructures used as photodetectors are described in [12], where the noise equivalent power (NEP) was achieved at $1.5 \text{ pW/Hz}^{0.5}$.

The development of photovoltaic THz quantum-cascade detectors (QCD) appears to be more promising. As compared with QWIP shifted structures, medium-infrared (IR) QCD show lower noise (due to the absence of dark current noise inherent in QWIP structures) and high-temperature operation capability. At the same time, in view of complicated numerical simulation of THz QCD band structure and carrier transport, only one research group has managed to implement THz QCD [13]. The authors have demonstrated detecting capability $\sim 5 \cdot 10^7 \text{ cm} \cdot (\text{Hz/W})^{0.5}$ at 3.5 THz and capability of operation at 50 K. In 2020, THz QCD simulation results were presented using Bayes optimization algorithm [14], Monte-Carlo together with genetic optimization algorithm [15]. These simulation

results were further developed in the medium-IR QCD field [16].

The first simulation and growing results for 2.5 THz quantum-cascade detector heterostructures by molecular beam epitaxy are described herein.

2. Experimental samples

The active region cascade period structure of 2.5 THz QCD was designed using commercial NextNano[®] software package [17] by iterative solution of Schrödinger–Poisson equation in $k \cdot p$ formalism for 4 K (see Fig. 1, *a*). Together with conductivity band profile, wave function squares in the designed cascade period layers are shown. The purpose of the structural design was to implement diagonal intersubband absorption in the „active“ quantum well (QW) layer (designated in Fig. 1, *a* as „active QW“). Quantum energy between 1–5 states was 10.2 meV, between 1–6 states was 11.7 meV and between 1–7 states was 15.3 meV.

After transitions from 1 state to 5–7 states, electrons are tunneled into the extractor region (carrier emission region). Layer parameters were improved in order to expand spatial overlap of the QW wave function envelope with the carrier emission region (2–4 states), extractor region (designated in Fig. 1, *a* as „extractor“). Only QWs within the extractor region are doped, which, on the one hand, ensures higher probability of electron relaxation (emission) into the extractor region (due to electron-impurity scattering) and, on the other hand, simultaneously decreases the probability of intersubband carrier relaxation in „active“ QW. As a result, this ensures increased efficiency of carrier transport between the cascade periods. QW doping level was chosen in such a way, on the one hand, to increase the probability of intersubband absorption in the „active“ QW, and, on the other hand, to avoid the last state in the extractor region

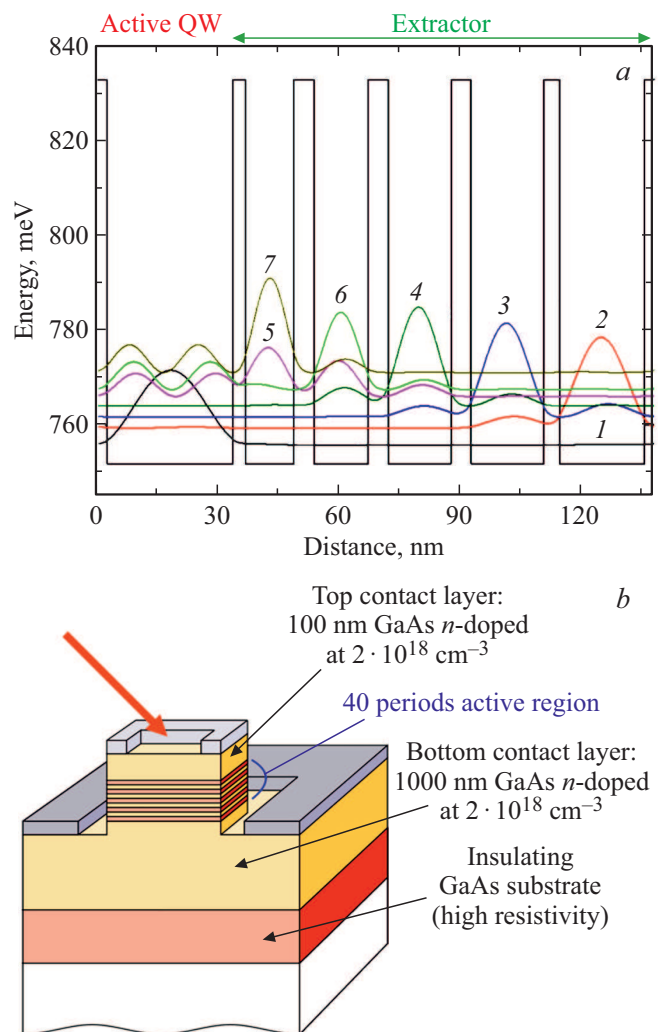


Figure 1. *a* — numerical calculation of wave function square in the 2.5 THz QCD cascade period; *b* — schematic diagram of the QCD crystal structure. The arrow shows incidence radiation at Brewster angle. (Colored version of the figure is presented in electronic version of the article).

Table 1. QCD heterostructure layer description

Material	Doping level, cm^{-3}	Thickness, Å
GaAs	$2 \cdot 10^{18}$	1000
$\text{Al}_{0.10}\text{GaAs}$		46
<u>GaAs</u>	$1 \cdot 10^{16}$	<u>210</u>
$\text{Al}_{0.10}\text{GaAs}$		40
<u>GaAs</u>	$1 \cdot 10^{16}$	<u>180</u>
$\text{Al}_{0.10}\text{GaAs}$		50
<u>GaAs</u>	$1 \cdot 10^{16}$	<u>155</u>
$\text{Al}_{0.10}\text{GaAs}$		50
<u>GaAs</u>	$1 \cdot 10^{16}$	<u>135</u>
$\text{Al}_{0.10}\text{GaAs}$		50
GaAs		120
$\text{Al}_{0.10}\text{GaAs}$		30
GaAs		312.5
$\text{Al}_{0.10}\text{GaAs}$		46
GaAs	$2 \cdot 10^{18}$	10000
GaAs substrate		350 μm

to be filled. For the detailed description of the QCD heterostructure layers, see Table 1. The active region and extractor region layers put in bold form one cascade period. The number of cascade periods is 40. The total layer thickness in the cascade period is 1378.5 Å. Underlined GaAs layers (in the extractor region) are silicon-doped (bulk doping).

QCD heterostructure was grown by molecular beam epitaxy (MBE). GaAs wafers with $(001) \pm 0.5^\circ$ orientation, conductivity type — semi-insulator (for decrease free carrier loss), were used as substrates. A $1 \mu\text{m}$ GaAs layer silicon-doped up to $n = 2 \cdot 10^{18} \text{ cm}^{-3}$ served as a lower contact layer. The active region included 40 cascade periods on the basis of the GaAs/ $\text{Al}_{0.1}\text{Ga}_{0.9}\text{As}$ solid solution heteropair. The total layer thickness in one cascade period was 137.9 nm. The top contact layer was formed on

the basis of GaAs with doping level $2 \cdot 10^{18} \text{ cm}^{-3}$. For the schematic diagram of the QCD crystal structure, see Fig. 1, *b*. A structure was chosen where the bottom contact was made to a heavily doped GaAs layer rather than to a doped substrate in order to reduce optical loss as a result of the use of a heavily doped substrate. The top contact is assumed to be formed as a frame along the meas perimeter to ensure sample illumination at Brewster angle.

To assess the structural quality of the QCD heterostructure, X-ray diffraction analysis and transmission electron microscopy (TEM) methods were used. TEM examinations were carried out using JEM2100F (Jeol, Japan) transmission electron microscope with accelerating voltage 200 kV. A standard cross-section sample preparation technique was used that is described, for example, in [18,19].

X-ray diffraction rocking curves were measured near (004) GaAs symmetric reflection using PANalytical X'PertPro diffractometer in the parallel X-ray beam geometry [18]. A tube with rotating copper anode ($\lambda = 0.15406 \text{ nm}$) is the 6 kW X-ray radiation source. The initial beam half-width did not exceed $12''$ due to the use of Ge (220) quadruplex slotted crystal monochrometer.

3. Results and discussion

Preliminary growth rate calibrations of GaAs and AlAs as well as $\text{Al}_{0.1}\text{Ga}_{0.9}\text{As}$ layer composition were carried out according to the data obtained by the X-ray diffraction method using a AlGaAs bulk layer test heterostructure. As a result, GaAs and AlAs growth rates were defined as 2.08 and 0.23 Å/s, respectively. For accurate calibration of thin layer thicknesses in the QCD cascade period, a test heterostructure equivalent to the QCD heterostructure, but with the number of cascade periods reduced down to 10, was grown immediately before the epitaxial growth. X-ray diffraction rocking curve $\Omega-2\theta$ was measured in the test heterostructure. High-order satellite peaks specific to the cascade period structure are observed on the curve. The analysis of satellite peak positions has shown that the average cascade period thickness was $139.0 \pm 6 \text{ nm}$, which is indicative of the growth specification deviation. Therefore, for adjustment of the cascade period thickness during epitaxial growth of the QCD heterostructure, the rate for gallium in the superstructure layers was increased from 2.08 to 2.11 Å/s within the growth program. The doping level was calibrated by the capacitance-voltage profiling method of thick GaAs:Si layer heterostructures.

The QCD heterostructure was grown at a substrate temperature of 575°C and III group materials and As flow ratio 1:10. The substrate temperature was controlled using the pyrometer readings calibrated at the start temperature of oxide removal from the GaAs substrate assumed equal to 590°C . The jig speed was 20 rpm which ensured more than 5 rotations during growth of the thinnest cascade period layer at the chosen growth rates. Thus, the best layer

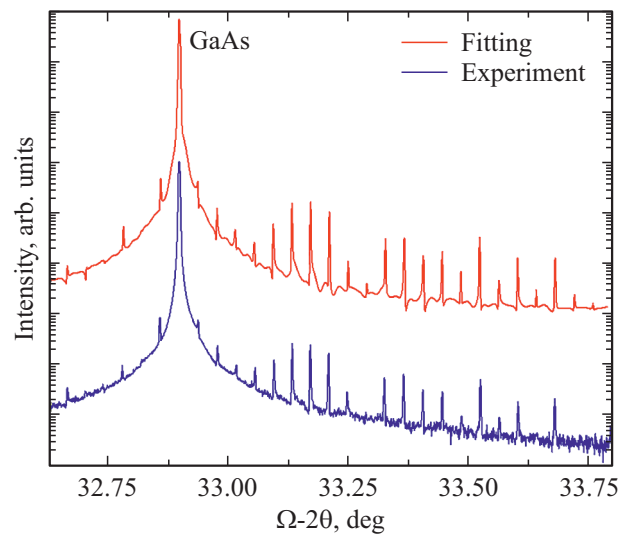


Figure 2. X-ray diffraction rocking curve of the QCD heterostructure measured in the wafer center (bottom curve) together with the numerical simulation results (top curve).

thickness homogeneity was ensured within the substrate area.

Figure 2 shows an X-ray diffraction rocking curve $\Omega-2\theta$ of the QCD heterostructure measured in the wafer center (bottom curve) together with the numerical simulation results. The rocking curve shows full coincidence of the satellite structure zero peak with the GaAs substrate peak position (designated as „GaAs“). This proves that the chemical composition of the epitaxial layers precisely match the chemical composition established in the growth specification. High-order satellite peaks (up to 21th order) are observed on the rocking curve. The curve analysis gives a sufficiently small average full width at half maximum (FWHM) for satellite peaks ($8.3 \pm 0.5''$) as compared with the previous results for similar QCL THz heterostructures on GaAs substrates ($13-19''$) [20–23], which is indicative of high boundary sharpness, constant cascade period and layer thickness, and of low roughness of heterointerfaces in the test heterostructure [23]. According to the positions of 10 satellite peaks, the average cascade period thickness was assessed and was equal to $135.0 \pm 2.0 \text{ nm}$, which correlates with the total cascade period layer thickness established in the growth specification (137.85 nm). The numerical approximation of all satellite peak positions gives an average cascade period thickness equal to 135.1 nm . The X-ray diffraction curves were measured at 25 mm from the substrate center. According to the simulation, the deviation of the average cascade period thickness did not exceed 1% as compared with the substrate center, which is indicative of a high layer homogeneity over the heterostructure surface. Thus, the X-ray diffraction analysis demonstrates high structural perfection of the produced QCD heterostructure and compliance of the layer thicknesses and compositions

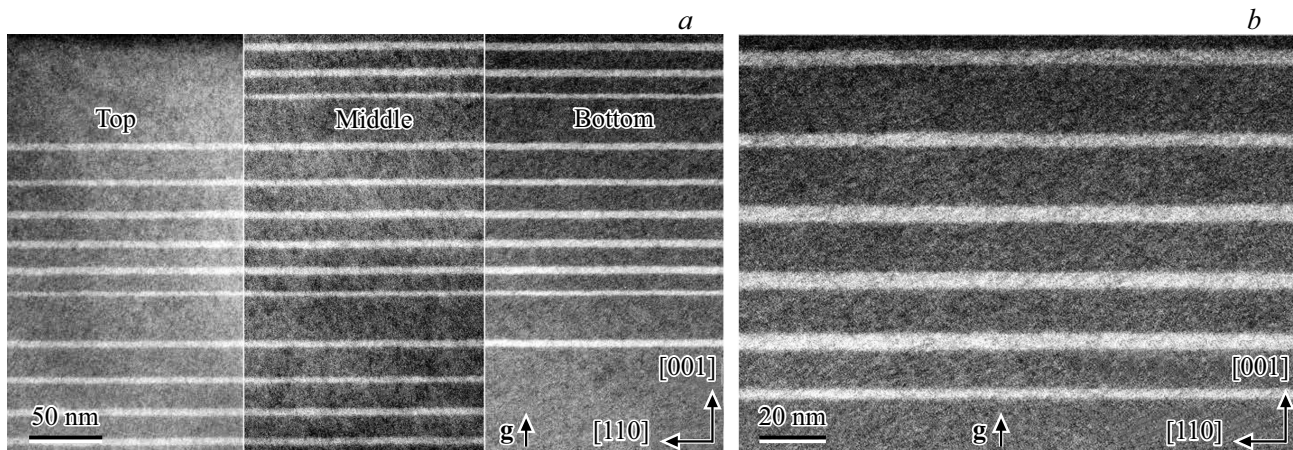


Figure 3. *a* — dark-field images of $(1\bar{1}0)$ sample cross-section in two-beam conditions with the active diffraction vector $g = (002)$ near the heterostructure surface (designated as „top“), in the center of the active region (designated as „middle“) and near the substrate (designated as „bottom“); *b* — dark-field image of the sample cross-section with the active diffraction vector $g = (002)$ in the center of the active region.

in the cascade periods with those established in the growth specification.

The review of the examination of dark-field TEM image of the sample cross-section $(1\bar{1}0)$ with $g = (002)$ near the substrate by transmission electron microscopy has shown that there are no boundaries between the substrate and the epitaxial layers. Figure 3, *a* shows TEM image of the cascade periods for three specific regions of the QCD heterostructure: near the heterostructure surface, in the center of the active region and near the substrate. Within the period, no differences in the layer thickness were observed and all cascade period layers have planar heteroboundaries that are shown on the enlarged image (see Fig. 3, *b*). The homogeneous layer thicknesses in the cascade periods do not change during the growth process, no extended defects were observed. Layer thicknesses in

the cascade period measured by the TEM image analysis are shown in Table 2. The total layer thickness in a cascade period was 137.3 ± 6.9 nm.

4. Conclusion

As a result of numerical simulation of a 2.5 THz quantum-cascade detector heterostructure by iterative solution of Schrödinger–Poisson equation in $k \cdot p$ formalism, the optimum layer thicknesses in the heterostructure active region were defined (quantum-cascade detector heterostructure design). Epitaxial growth conditions were tested by the molecular beam epitaxy of the QCD heterostructures in accordance with the proposed QCD design. The X-ray diffraction analysis and transmission electron microscopy demonstrate high structural perfection of the produced heterostructure and compliance with the QCD design.

Table 2. Layer thickness measurements in the cascade period by TEM method. The instrument error is $\pm 5\%$ according to the measurement procedure

Material	Design thickness, Å	TEM measured thickness, Å
GaAs	210	210
Al _{0.1} Ga _{0.9} As	40	42
GaAs	180	180
Al _{0.1} Ga _{0.9} As	50	50.2
GaAs	155	154
Al _{0.1} Ga _{0.9} As	50	50.2
GaAs	135	133
Al _{0.1} Ga _{0.9} As	50	50.2
GaAs	120	117
Al _{0.1} Ga _{0.9} As	30	29.7
GaAs	312.5	312
Al _{0.1} Ga _{0.9} As	46	45.1

Funding

The research was supported by a financial grant provided by the Russian Science Foundation (project No. 20-79-10285).

Conflict of interest

The authors declare that they have no conflict of interest.

References

- [1] L. Consolino, S. Bartalini, H. Beere, D. Ritchie, M. Vitiello, P. De Natale. *Sensors*, **13** (3), 3331 (2013).
- [2] G.-R. Kim, T.-I. Jeon, D. Grischkowsky. *Opt. Express*, **25** (21), 25422 (2017).

- [3] M. Locatelli, M. Ravaro, S. Bartalini, L. Consolino, M.S. Vitiello, R. Cicchi, F. Pavone, P. De Natale. *Sci. Rep.*, **5**(1), 13566 (2015).
- [4] N. Rothbart, O. Holz, R. Koczulla, K. Schmalz, H.-W. Hübers. *Sensors*, **19**(12), 2719 (2019).
- [5] P.U. Jepsen, D.G. Cooke, M. Koch. *Laser Photon. Rev.*, **5**(1), 124 (2010).
- [6] A. Khalatpour, A.K. Paulsen, C. Deimert, Z.R. Wasilewski, Q. Hu. *Nature Photonics*, **15**(1), 16 (2020).
- [7] A. Vardi, N. Kheirodin, L. Nevou, H. Machhadani, L. Vivien, P. Crozat, M. Tchernycheva, R. Colombelli, F.H. Julien, F. Guillot, C. Bougerol, E. Monroy, S. Schacham, G. Bahir. *Appl. Phys. Lett.*, **93**(19), 193509 (2008).
- [8] M. Hakl, Q. Lin, S. Lepillet, M. Billet, J.-F. Lampin, S. Pirotta, R. Colombelli, W. Wan, J.C. Cao, H. Li, E. Peytavit, S. Barbieri. *ACS Photonics*, **8**(2), 464 (2021).
- [9] D. Palaferri, Y. Todorov, Y.N. Chen, J. Madeo, A. Vasanelli, L.H. Li, A.G. Davies, E.H. Linfield, C. Sirtori. *Appl. Phys. Lett.*, **106**(16), 161102 (2015).
- [10] H. Li, W.-J. Wan, Z.-Y. Tan, Z.-L. Fu, H.-X. Wang, T. Zhou, Z.-P. Li, C. Wang, X.-G. Guo, J.-C. Cao. *Sci. Rep.*, **7**(1), 3452 (2017).
- [11] B. Paulillo, S. Pirotta, H. Nong, P. Crozat, S. Guilet, G. Xu, S. Dhillon, L.H. Li, A.G. Davies, E.H. Linfield, R. Colombelli. *Optica*, **4**(12), 1451 (2017).
- [12] P. Micheletti, J. Faist, T. Olariu, U. Senica, M. Beck, G. Scalari. *APL Phot. Optica*, **6**, 106102 (2021).
- [13] M. Graf, G. Scalari, D. Hofstetter, J. Faist, H. Beere, E. Linfield, D. Ritchie, G. Davies. *Appl. Phys. Lett.*, **84**(4), 475 (2004).
- [14] J. Popp, M. Haider, M. Franckie, J. Faist, C. Jirauschek. In: *2020 Int. Conf. on Numerical Simulation of Optoelectronic Devices (NUSOD)* (Turin, Italy, 2020). doi: 10.1109/NUSOD49422.2020.9217784
- [15] J. Popp, M. Haider, M. Franckie, J. Faist, C. Jirauschek. In: *2020 XXXIIIrd General Assembly and Scientific Symposium of the Int. Union of Radio Science* (Rome, Italy, 2020). doi: 10.23919/URSIGASS49373.2020.9232167
- [16] J. Popp, M. Haider, M. Franckie, J. Faist, C. Jirauschek. *Opt. Quant. Electron.*, **53**(6), 287 (2021).
- [17] link: <https://www.nextnano.de/>. Accepted date: 21.09.2021.
- [18] A.V. Babichev, V.V. Dudelev, A.G. Gladyshev, D.A. Mikhailov, A.S. Kurochkin, E.S. Kolodeznyi, V.E. Bougrov, V.N. Nevedomskiy, L.Y. Karachinsky, I.I. Novikov, D.V. Denisov, A.S. Ionov, S.O. Slipchenko, A.V. Lutetskiy, N.A. Pikhtin, G.S. Sokolovskii, A.Y. Egorov. *Techn. Phys. Lett.*, **45**(7), 735 (2019).
- [19] A.V. Babichev, A.S. Kurochkin, E.C. Kolodeznyi, A.V. Filimonov, A.A. Usikova, V.N. Nevedomsky, A.G. Gladyshev, L.Y. Karachinsky, I.I. Novikov, A.Y. Egorov. *Semiconductors*, **52**(6), 745 (2018).
- [20] A.E. Zhukov, G.E. Cirlin, R.R. Reznik, Y.B. Samsonenko, A.I. Khrebtov, M.A. Kaliteevski, K.A. Ivanov, N.V. Kryzhanovskaya, M.V. Maximov, Z.I. Alferov. *Semiconductors*, **50**(5), 662 (2016).
- [21] G.E. Cirlin, R.R. Reznik, A.E. Zhukov, R.A. Khabibullin, K.V. Maremyanin, V.I. Gavrilenko, S.V. Morozov. *Semiconductors*, **54**(9), 1092 (2020).
- [22] H.E. Beere, J.R. Freeman, O.P. Marshall, C.H. Worrall, D. Ritchie. *J. Cryst. Growth*, **311**(7), 1923 (2009).
- [23] X. Wang, C. Shen, T. Jiang, Z. Zhan, Q. Deng, W. Li, W. Wu, N. Yang, W. Chu, S. Duan. *AIP Adv.*, **6**(7), 075210 (2016).